Global and Planetary Change 236 (2024) 104413

Contents lists available at ScienceDirect

Global and Planetary Change

journal homepage: www.elsevier.com/locate/gloplacha

iLOSCAR: interactive Long-term Ocean-atmosphere-Sediment CArbon cycle Reservoir model v1.0

Shihan Li [a], Richard E. Zeebe [b], Shuang Zhang [a,*]

[a] Department of Oceanography, Texas A&M University, College Station, TX 77843, USA
[b] School of Ocean and Earth Science and Technology, University of Hawaii at Manoa, Honolulu, HI 96822, USA

ARTICLE INFO

Editor: Dr. Maoyan Zhu

Keywords:
Carbon cycle model
Geological hyperthermal events
Double-inversion algorithm
Carbon emission trajectory

ABSTRACT

Computationally inexpensive carbon cycle models serve as critical and efficient tools for illuminating the complex dynamics of the carbon cycle and its interplay with the climate system, offering insights into how our planet has responded to climate perturbations throughout its history. During geologic hyperthermal events, carbon cycle models are employed to trace the trajectory of carbon emissions and establish a connection between the emission trajectory and changes in the Earth's surface environment. To date, the prevalent method to estimate the carbon emission rate relies on coupling the carbon cycle modeling and proxy reconstructions. Most previous studies employ a forward methodology, i.e., they force the model with an array of predefined carbon injection scenarios and select the one that produces the best fit to one or more specific proxy-derived records (e.g., atmospheric pCO_2, sea surface pH, and calcite compensation depth) as the optimal solution. However, this forward method has two potential disadvantages. First, it can be computationally expensive, particularly when tens of thousands of scenarios need to be conducted to find the best solution. Second, it might not yield the best injection trajectory if none of the predefined carbon emission curves represents the realistic emission curve. Hence, an inverse model that can reconstruct the carbon emission trajectory directly from the record/records is urgently needed. In this study, building upon the Long-term Ocean-atmosphere-Sediment CArbon cycle Reservoir (LOSCAR) Model (Zeebe, 2012), we develop an interactive carbon cycle model (named iLOSCAR) using the open-source Python language and include two options, a forward model and an inverse model. The forward model replicates the original LOSCAR model, while the inverse model calculates the emission trajectory constrained by the proxy records in a single run. Both models are accessible via a web-based interface, which allows users to interactively tune model parameters and conduct experiments. In this paper, we present the details of iLOSCAR, including model structure and derivation of key equations. We then validate iLOSCAR's performance through an identical twin test and model intercomparison. We also apply it to a climatic perturbation event to diagnose features of the emission pattern that were overlooked in previous studies. Finally, we discuss the possible directions for model's future development.

1. Introduction

Since the beginning of the industrial era, anthropogenic carbon emissions have resulted in the continuous increase in atmospheric CO_2 concentration (pCO_2), from ~280 in the pre-industry world to ~410 ppm in 2019 (Legg, 2021). The rapidly rising pCO_2 levels are altering the radiative balance of the Earth's surface and the mean global surface temperature is ~1 °C higher in 2011–2020 than 1850–1900 (Morice et al., 2021). Continuing carbon emission also impacts the ocean carbonate system, causing the decline in surface pH and the reduction in the ocean's carbonate mineral saturation state (Hönisch et al., 2012). The global warming and ocean acidification are suggested to bring about negative consequences for marine life (Zeebe et al., 2008). As such, forecasting the future pCO_2 trend and attendant response of Earth system has become a high priority for the scientific community. However, model simulations for future climate projections still have large uncertainties, partly due to the poor understanding and parameterizations of the global carbon cycle (Goddéris et al., 2023; Legg, 2021). Although no perfect analogs for the ongoing perturbation exist, transient warming events accompanied by global carbon cycle perturbation are rather

* Corresponding author.
E-mail address: shuang-zhang@tamu.edu (S. Zhang).

https://doi.org/10.1016/j.gloplacha.2024.104413
Received 29 September 2023; Received in revised form 23 January 2024; Accepted 9 March 2024
Available online 11 March 2024

common in Earth's history and have been explored to provide insight to the ongoing climate change (Foster et al., 2018). Moreover, achieving a more precise delineation of carbon emission trajectories during these geological hyperthermal events can enrich our holistic understanding of the temporal interplay between the carbon cycle and changes in Earth's surface environment (Zeebe et al., 2016), which is crucial for predicting future environmental conditions under different scenarios of anthropogenic carbon emissions. Consequently, this enhanced comprehension would be instrumental in shaping our responses to potential climatic changes and in steering future mitigation strategies.

To date, the carbon emission trajectory for the past events is predominantly derived through coupling the carbon cycle modeling and proxy reconstructions. Previous studies have primarily utilized a forward methodology, in which one forces the model with an ensemble of predefined carbon injection scenarios and then selects the scenario that produces the best fit to one or more specific proxy-derived records as the optimal solution (Chen et al., 2022; Clarkson et al., 2018; Dunkley Jones et al., 2018; Hull et al., 2020; Landwehrs et al., 2020; Papadomanolaki et al., 2022a; Wang et al., 2023; Zeebe et al., 2009). However, the forward method is associated with several potential disadvantages. Firstly, it can be computationally expensive, particularly when tens of thousands of scenarios need to be conducted to find the best solution (Chen et al., 2022). Additionally, the predefined emission scenarios are usually set to follow a specific type of distribution, e.g., uniform distribution (Harper et al., 2020; Hull et al., 2020; Papadomanolaki et al., 2022a), beta distribution (Chen et al., 2022), gamma distribution (Shen et al., 2022b), or Gaussian distribution (Shen et al., 2022a). However, carbon emissions in the real world may occur spontaneously and thus be randomly distributed. Therefore, the forward method may not necessarily yield the best realistic injection trajectory. Furthermore, proxy records suggest that carbon emissions during certain hyperthermal events are characterized with several carbon emission pulses (e.g., the Permian-Triassic boundary, PTB, and the Paleocene-Eocene Thermal Maximum, PETM, events; Bowen et al., 2015; Wu et al., 2023). Such a discretized emission pattern is challenging to be resolved with the forward method, which precludes a comprehensive understanding of how carbon emissions evolve in time.

Recently, a double inversion method has been developed, building upon the cGENIE Earth system model (Edwards and Marsh, 2005; Ridgwell et al., 2007). This method facilitates the direct calculation of both the time-resolved mass and provenance (i.e., isotopic composition) of emitted carbon from given proxy records during hyperthermal events (Cui et al., 2011). For instance, when using pCO_2 data (or ocean surface pH) to constrain the emission rate, the inverse cGENIE model adjusts the mass of carbon input automatically at each model time-step (usually one week) to reproduce the given pCO_2 value. If the model value falls below (above) the data value, a pulse of carbon with a prescribed mass will be released to (removed from) the atmosphere (Cui et al., 2011). Similarly, the $\delta^{13}C$ value of emitted carbon is also adjusted at each step to match the given surface ocean $\delta^{13}C$. The model can then estimate the time-resolved carbon emission scenario by binning the emission fluxes and isotopic value in time. This inversion method has been applied to quantify the carbon emission scenario over the Paleocene-Eocene Thermal Maximum event (PETM, ~ 56 Ma; Gutjahr et al., 2017), Oceanic Anoxic Event 1a (~121 Ma; Adloff et al., 2020), and the Permian-Triassic Boundary (PTB, ~252 Ma; Wu et al., 2023).

Although significant improvement has been made compared with the forward method, the current double-inversion algorithm is limited in its wider application due to its low computational efficiency and operational difficulty, particularly for scientists lacking programming and computer skills. Furthermore, modeling studies pertaining to deep time are often limited by the absence of well-defined parameters for relevant processes in the carbon cycle. To address this, recent studies have employed Monte Carlo simulations, which involve randomly selecting thousands of ensembles of model parameters from predefined distributions, to achieve comprehensive error propagation (Chen et al., 2022; Isson et al., 2022; Krissansen-Totton and Catling, 2017, 2020). However, the cGENIE model's limited computational efficiency poses a challenge to conducting sensitivity tests that explore the impact of uncertainties linked to key carbon cycle parameters on modeled emission scenarios. Such parameters include, but are not limited to, background silicate and carbonate weathering flux and corresponding isotopic signature, marine rain ratio, and climate sensitivity. For instance, in Wu et al. (2023), only 15 experiments are conducted to test the sensitivity of modeling results on the uncertainties of proxy data, whereas the dependency on the aforementioned parameters is not explored.

Therefore, it is critical to have an efficient inverse model that can reliably reconstruct the trajectory of carbon emissions constrained by proxy records. To address this need, we have developed iLOSCAR, an extension of the LOSCAR model (Zeebe, 2012). Originally designed for efficiently computing global carbon cycle dynamics in a forward way, LOSCAR has been widely used to estimate carbon emissions during various hyperthermal events (Zeebe et al, 2009; Chen et al., 2022; Cox and Keller, 2023; Heimdal et al., 2020; Henehan et al., 2020; Hull et al., 2020; Papadomanolaki et al., 2022b). Our newly developed iLOSCAR leverages LOSCAR's modeling capabilities, and allows for both forward and inverse modeling. iLOSCAR can complete the double inversion in ~10 min on a current standard laptop machine with Apple M1 8 cores @3.2 GHz, and yield results comparable to those from previous studies using the more complex cGENIE model (see examples in Section 4 and 5, Table 1). Additionally, our model features a user-friendly web-based interface, enabling users to interactively tune model parameters and conduct experiments. This intuitive design eliminates the necessity for extensive programming knowledge, making complex modeling accessible to a broader user base. Furthermore, the iLOSCAR code is published as an open-source Python package, allowing other scientists to contribute to the model development freely and collaboratively. For example, users can couple other elemental cycles such as P and Ca (Komar and Zeebe, 2016, 2017) into iLOSCAR in future versions to handle a wider range of environmental and geological scenarios.

In the following, we will present the details of iLOSCAR, including model structure and the inversion algorithm in Section 2. Section 3 and 4 will focus on validating the model's performance through an identical twin test and model intercomparison. We will then use the model to refine the estimate of carbon emission trajectory during a climatic perturbation event in the paleo-glacial world (Kasimovian–Gzhelian boundary, KGB; ~304 Ma) and discuss some features of the emission pattern that were overlooked before. Finally, we will discuss the model's limitations and potential directions for the model's future development.

2. Model description

2.1. Forward model

The numerical architecture and parameterizations of the forward model in iLOSCAR are based on the original LOSCAR model (Zeebe, 2012), which comprises three components: atmosphere, ocean, and sediment. The oceanic component of the model is segmented into three ocean reservoirs in the modern version: the Atlantic, Indian, and Pacific. In the paleo version, an additional fourth reservoir, the Tethys, is included. Each of these reservoirs is further subdivided into three depth zones: surface, intermediate, and deep. Furthermore, the model includes a generic box that parameterizes the high latitude ocean. The forward model tracks various biogeochemical tracers, including oceanic dissolved inorganic carbon-DIC, total alkalinity-ALK, stable carbon isotopes-^{13}C, atmospheric pCO_2, and others, in different boxes. These tracers form the state variables ($\vec{y}$) of the model. Their dynamic changes over time are governed by the following ordinary differential equation (ODE) system:

$$\frac{d\vec{y}}{dt} = F(t, \vec{y}) \quad (1)$$

Table 1
Summary of double-inversion experiments.

Event	Cumulative emission (Gt)		Peak Emission rate (Gt/yr)		Average $\delta^{13}C$ (‰)		Running time (minutes)[a]
	This study	From Ref.	This study	From Ref.	This study	From Ref.	
PTB Phase 1	4955	5014	0.14	0.2	−14.6	−16	13.6
PTB Phase 2	20,538	20,984	0.69	0.7	−7.7	−9	
KGB1	9106	9000	0.025	–	−18.2	−19	7

[a] Time for running the model from the web-based interface on a current standard laptop machine with Apple M1 8 cores @3.2 GHz (no other CPU-demanding processes running).

where t is time, and F is the function used to calculate the derivatives of the state variables $\vec{y}$. The dimension of $\vec{y}$ is 140 (modern setup) or 184 (palaeo setup). Note that the information of model parameters is implicitly incorporated in the function *F*, including the time-dependent carbon emission scenario (termed as $fcinp(t)$) and the isotopic composition of emitted carbon ($f\delta^{13}C(t)$). The equations and corresponding processes encapsulated within function *F* have been described in detail by Zeebe (2012). In this context, we will treat F as a known function. Then the task of the forward model is to solve the ODE system with initial state values of $\vec{y}(t_0)$:

$$\vec{y}(t) = \vec{y}(t_0) + \int_{t_0}^{t} F\left(\tau,\ \vec{y}(\tau)\right) d\tau \tag{2}$$

In comparison to the original LOSCAR model, our iLOSCAR forward model features several innovations. Firstly, iLOSCAR is implemented using the open-source Python language. This grants access to a broader suite of advanced computational packages compared to the C language utilized by the original LOSCAR model. Secondly, to address the reduction of running speed caused by switching the programming language, the codes are optimized using Numba, a Just-In-Time (JIT) compiler, to enhance the model's computational speed and efficiency. Also, the original function used for calculating the oceanic carbonate system (Follows et al., 2006) has been vectorized. This modification allows simultaneous calculations from multiple inputs, enhancing computational efficiency. Lastly, we employ the LSODA (an acronym for Livermore Solver for Ordinary Differential equations, with Automatic method switching for stiff and nonstiff problems) algorithm as the ODE solver, given its demonstrated stability when dealing with stiff problems, as highlighted by Hindmarsh (1992).

2.2. Inverse model

2.2.1. Inverse algorithm

As aforementioned, the aim of the inverse model is to derive $fcinp(t)$ and $f\delta^{13}C(t)$ that can force the model to make the best fit to proxy-derived records $x_{obs}(t)$. The best fit here is defined as the minimum of the sum of relative errors between $x_{obs}(t)$ and corresponding modeling results $x_{model}(t)$:

$$fcinp(t), f\delta^{13}C(t) = argmin\sum_{i=1}^{n}\left|\frac{x_{model}(t_i) - x_{obs}(t_i)}{x_{obs}(t_i)}\right| \tag{3}$$

In this case, $fcinp(t)$ and $f\delta^{13}C(t)$ are implicit variables in $x_{model}(t_i)$. Previous double-inversion studies based on cGENIE select pCO_2 or average sea surface pH (pH_{as} hereinafter) and average sea surface $\delta^{13}C$ ($\delta^{13}C_{as}$ hereinafter) to determine the $fcinp(t)$ and $f\delta^{13}C(t)$ (Gutjahr et al., 2017; Wu et al., 2023). The dynamic evolution of these three proxies is also resolved by iLOSCAR, and therefore we offer the same options for double inversion in our inverse model.

Although theoretically carbon emissions in the geologic past could be intermittent, it is necessary to make some assumptions to reduce the number of parameters required to describe $fcinp(t)$ and $f\delta^{13}C(t)$. Here a stepwise uniform function is applied to represent the emission trajectory. Specifically, the modeled time period is partitioned into a specific number of intervals according to provided x_{obs} data. In each interval, we assume a constant emission rate, i.e.:

$$\begin{aligned} fcinp(t) &= k_1\ (if\ t_0 \le t \le t_1) \\ &= k_2\ (if\ t_1 < t \le t_2) \\ &\cdots\cdots \\ &= k_n\ (if\ t_{n-1} < t \le t_n). \end{aligned} \tag{4}$$

A similar function is used to represent $\delta^{13}C(t)$:

$$\begin{aligned} f\delta^{13}C(t) &= d_1\ (\ if\ t_0 \le t \le t_1) \\ &= d_2\ (if\ \ t_1 < t \le t_2) \\ &\cdots\cdots \\ &= d_n\ (if\ t_{n-1} < t \le t_n) \end{aligned} \tag{5}$$

where $t_{i\ldots n}$ are determined from given target proxy records. In this way, $fcinp(t)$ and $f\delta^{13}C(t)$ can be represented by *n* parameters. Then we apply a sequential iteration algorithm to solve the inverse problem by deriving $k_1 \ldots k_n$ and $d_1 \ldots d_n$, which is described as follows:

(1) Turn off the carbon emission and spin up the forward model for 2 million years to the steady state. Tune the parameters until initial $x_{model} = x_{obs}(t_0)$. *x* here could be pH_{as} or pCO_2, according to the proxy data given.
(2) Start from the $(t_0, t_1$ interval and k_1 is the only unknown parameter for the defined cost function (Eq. (3)) at this interval.
(3) Apply numerical methods to solve k_1 (see Section 2.2.2).
(4) Run the forward model at the $(t_0, t_1$ interval with the k_1-based $fcinp(t)$, then save the $\vec{y}(t_1)$ as the initial $\vec{y}$ values for the next interval (t_1, t_2).
(5) Move to the next interval and repeat step 2, 3, and 4. Stop the iteration when k_n is determined.
(6) Repeat steps 2–5 to calculate $(d_1, \ldots, d_n)$ for $f\delta^{13}C(t)$. The proxy data used in this step will be $\delta^{13}C_{as}$.

2.2.2. Numerical methods to solve k and d

Step 3 is a critical component of our inversion algorithm. At each iteration, one new *k* or *d* will be solved for defining the emission trajectory. Consequently, the solution to the optimization problem specified in Eq. (3) will be the root of the following equation:

$$x_{model}(t_i) = x_{obs}(t_i) \tag{6}$$

To find the root of Eq. (6), we apply the TOMS 748 root-finding algorithm, which uses a mixture of inverse cubic interpolation and Newton-quadratic steps to enclose zeros of contiguous univariate functions (Alefeld et al., 1995). This algorithm offers the advantage of a rapid convergence rate, which significantly accelerates the inversion process. Additionally, Algorithm 748 is readily available in the Python Scipy package.

3. Test

Before applying the model to the case studies, we validate its performance through various tests.

3.1. Forward model test

To assess the performance of the forward model, we compare the modeling outcomes obtained from both iLOSCAR and the original LOSCAR model. These comparisons are made under both modern and paleo default settings, using the same simulated carbon emission trajectory of 1000 Gt carbon (1Gt = 10^{15} g; −55‰ $\delta^{13}C$) over 6 kyr (as depicted in Fig. S1 and S2). Each experiment runs for a duration of 100 kyr. We use the LOSCAR modeling results as the baseline, and conduct timepoint-wise comparisons for two key proxies, namely, pCO_2 and $\delta^{13}C$ of atmospheric CO_2. The relative difference between the two models for these proxies is in the order of 10^{-4} to 10^{-5}, which may be attributed to the difference between the ODE integration methods applied: a fourth-order Rosenbrock method in LOSCAR, while an LSODA method in iLOSCAR. The carbon content and isotope values in different boxes are closely interlinked. Therefore, the robust alignment of these two proxies between both models attests to the reliability of iLOSCAR's forward model. To further substantiate our conclusion, we supply the same $\vec{y}$ and t to the ODE system represented by Eq. (2). We find that the difference between the derivatives computed by the two models is of the order of 10^{-16}, which is close to machine precision, thus corroborating the reliability of our newly developed iLOSCAR model.

Moreover, the iLOSCAR forward model is efficient. The reported time below is from running the model from the web-based interface on a current standard laptop machine featuring a Mac operating system and Apple M1 8 cores @3.2 GHz, without any concurrent high-demand CPU processes. For the 100 kyr test, in the context of our modern and paleo experiments previously discussed, the model takes around 18 and 22 s respectively, with Numba compilation consuming roughly 13 to 16 s of this time. Notably, the compilation process is only necessary during iLOSCAR's initial execution. Once compiled, subsequent perturbation experiments are significantly expedited, taking merely ~5 and ~ 6 s to complete. While this might be slightly slower than the original LOSCAR model (which operates in ~2 s), the computational efficiency of iLOSCAR remains robust, meeting the requirements of most potential applications. A comprehensive and detailed description of the comparison tests can be found in the Supplementary Materials.

3.2. Inverse model test

An identical twin test is performed to assess the performance of the inverse model. In this test, a preliminary run of the forward model is used to generate a synthetic 'truth' proxy data set, which is subsequently used in the inverse model experiments. Thus, the twin test provides a straightforward way to check whether the inverse algorithm works correctly. During the experiment, we prescribe an artificial emission curve with a two-stage pattern (Fig. 1). Specifically, 3000 Gt ^{13}C-depleted carbon (−20‰ $\delta^{13}C$, equivalent to the $\delta^{13}C$ of typical sedimentary organic carbon) is emitted to the atmosphere over the first 3000 years, simulating a swift and brief ejection event. This is followed by a release of 10,000 Gt carbon (−5 ‰ $\delta^{13}C$, equivalent to the $\delta^{13}C$ of mantle-dominated CO_2 degassing) over 35,000 years. The maximum emission rates reach 2.1 and 0.5 Gt/yr in these two respective events,

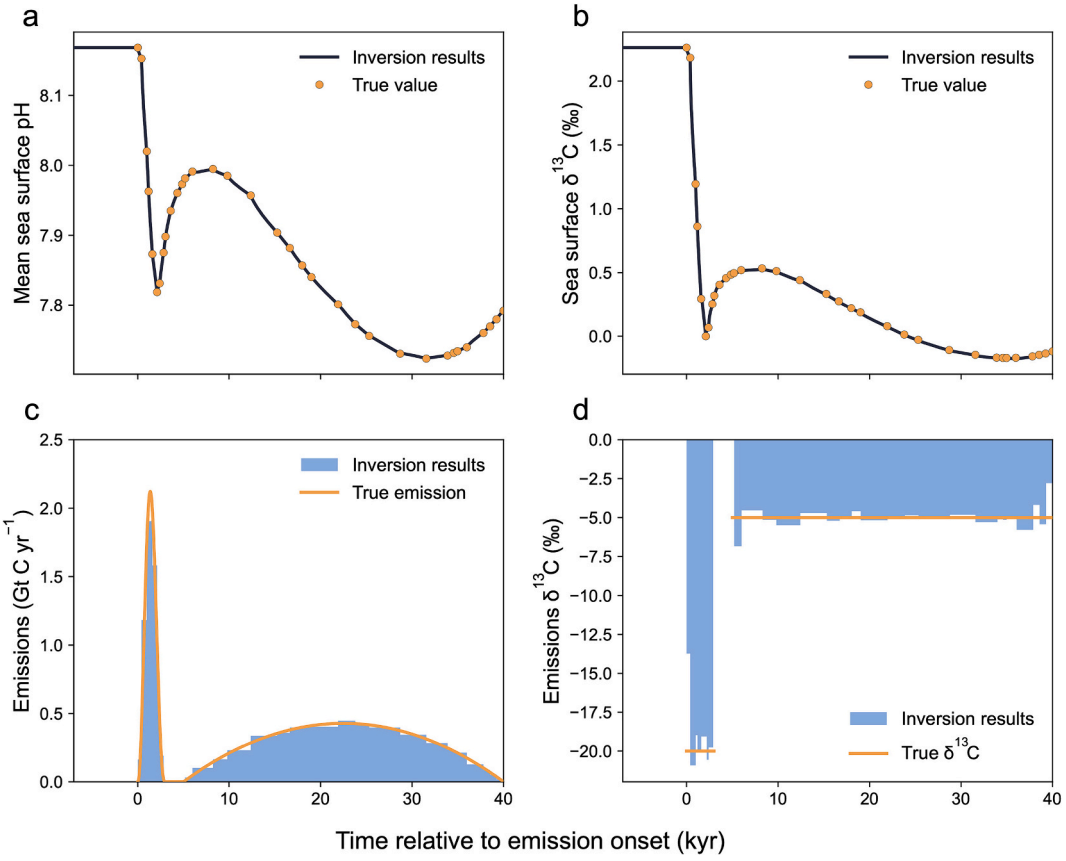

Fig. 1. Twin test results for the inverse model. a, b, Modeled global mean ocean surface pH and $\delta^{13}C$. Yellow symbols denote the target proxy records with the prescribed carbon emission scenario, which is shown in c (emission rate) and d (isotopic value). The blue bars in b and d represent the recovered emission trajectory (carbon emission rate and carbon isotope value) from the inverse model. (For interpretation of the references to colour in this figure legend, the reader is referred to the web version of this article.)

encapsulating the known range of the previous estimates for past hyperthermal events (Gutjahr et al., 2017; Wu et al., 2023).

The inverse model results, constrained by both the pH and $\delta^{13}C_{as}$ records generated by the forward model, are shown in Fig. 1. These results suggest a total carbon release of approximately 12,987 Gt, a value very close to the actual amount of 13,000 Gt. The pulsive pattern is also resolved by the model, with emissions concentrated within two distinct time intervals. The reconstructed largest emission rate in the first stage is ~1.9 Gt/yr, slightly lower than the predefined value (~2.1 Gt/yr). The small difference could be attributed to undersampling near the time when the largest emission rate occurs (Fig. 1c). The reconstructed $\delta^{13}C$ shows some oscillation when carbon input is slow (e.g., first 500 years), which could be corrected by weighted average $\delta^{13}C$ calculation over a specific time (Fig. 1d). The mean $\delta^{13}C$ for the first 3 kyr and the 5–40 kyr interval are −19.77‰ and − 5.03‰, respectively, similar to the true values. In summary, the inverse model successfully recovers the prescribed carbon emission trajectory.

Following the validation of the model's performance, we proceed to apply the inverse model to investigate two warming events in Section 4 and 5, namely PTB and KGB. Both events are characterized by significant negative carbon isotope excursions (CIE) and are closely linked to perturbations of the carbon cycle (Chen et al., 2022; Wu et al., 2021). In each experiment, the model parameters are first fine-tuned to match the boundary conditions as detailed in the Supplementary materials. Then, the published proxy records are used to constrain the inverse model to reconstruct the carbon emission trajectories, thereby offering insights into the underlying carbon cycle dynamics of these significant climatic events.

4. Model intercomparison: emission trajectory reconstruction across the PTB

The PTB records an extreme global warming of approximately 7 °C to 10 °C, and the largest mass extinction in the Phanerozoic (Fan et al., 2020; Sun et al., 2012). Previous double inversion results indicate massive carbon emissions across the PTB (~ 25,000 Gt), and the emission trajectory shows a two-phase pattern (Fig. 2c). For our current iLOSCAR inverse model runs, the pCO_2 and $\delta^{13}C_{as}$ records were taken from Wu et al., 2021, 2023.

The double-inversion experiment generates an emission trajectory that aligns well with previous estimates and successfully reconstructs the two-phase pattern across the PTB (Fig. 2; Table 1). The slight differences are considered acceptable, considering the variance in the parameterization of many processes between the two models, such as the organic carbon cycle in the ocean, the internal ocean mixing rates, and the calcite burial on the seafloor (Ridgwell et al., 2007; Ridgwell and Hargreaves, 2007; Zeebe, 2012). The calculated $\delta^{13}C_{source}$ values during two phases are both slightly higher by ~1.3‰ than those from Wu et al. (2023), with an average of −14.6 ‰ (0–52 kyr) and − 7.7‰ (52–94 kyr), respectively. Despite the minor discrepancy, the results still illustrate a transition from a mixed thermogenic and volcanic carbon source to a more mantle-dominated volcanic source, as suggested in Wu et al. (2023). Concurrently, the diagnosed cumulative carbon emissions associated with the two phases show negligible difference between this study and Wu et al. (2023) (Fig. 2c; Table 1). Our model predicts a transient sea surface warming of 7.5 °C and a 0.45 unit decrease of ocean surface pH. Of these changes, only an approximate 1.8 °C temperature rise and a 0.11 unit pH decrease occur during Phase 1(Fig. 2a).

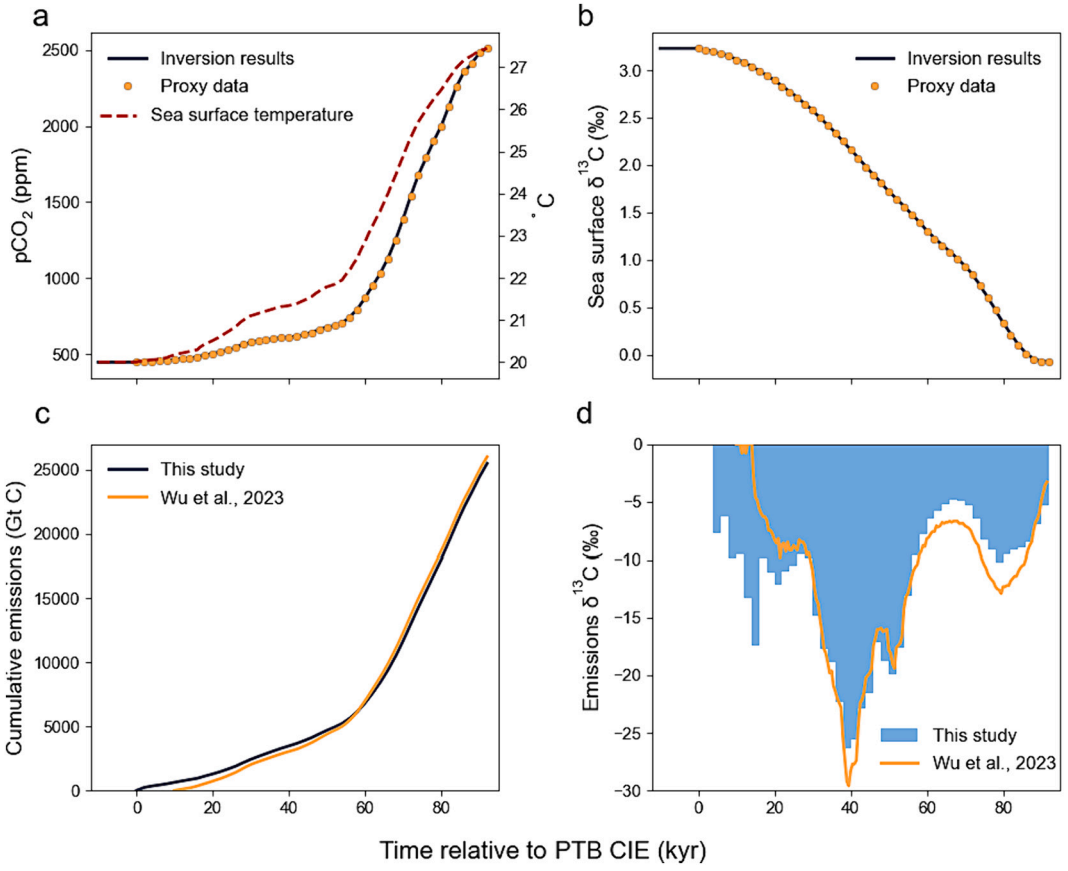

Fig. 2. Modeling results across the PTB. a, b, Modeling pCO_2, sea surface temperature and $\delta^{13}C$ results from the inversion-derived carbon emission trajectories (lines). Yellow symbols in a and b denote the smoothing proxy records, which are used as input in the iLOSCAR inverse model (Wu et al., 2021, 2023). $\delta^{13}C_{as}$ data in b is derived from the compilation of global marine carbonate $\delta^{13}C$ data (Wu et al., 2023). c, d, Inversion results comparison between this study and the standard run in Wu et al. (2023). (For interpretation of the references to colour in this figure legend, the reader is referred to the web version of this article.)

Our inverse modeling results also underscore the advantages of inverse- over brute-force forward operations of carbon cycle models. For instance, while the forward modeling using LOSCAR (Wang et al., 2023) successfully reconstructs the average environmental change and carbon emission pattern during the Permian-Triassic boundary (PTB), it lacks the ability to discern the two-phase pattern.

5. Recalculating the emission trajectory across the KGB

The KGB is a global warming event that occurs during a paleo-glacial state with a modern-like background pCO_2 value (~350 ppm) (Chen et al., 2022). Thus, the KGB study is expected to provide more insight into the current climate change and its impact on Earth's environment. However, the carbon release trajectory during the KGB is primarily obtained using a brute-force forward modeling approach with the original LOSCAR model (Chen et al., 2022). As a result, the reconstructed carbon emission trajectory may not mirror the actual solution. Here we implement the inverse model to improve upon the previous estimates, aiming to enhance our understanding of the trigger and recovery mechanisms associated with this warming event.

An injection of ~9000 Gt organic matter-derived C is postulated to explain the observed pCO_2 and $\delta^{13}C_{as}$ excursion (Chen et al., 2022). In this study, we employ the same pCO_2 and $\delta 13C_{as}$ records from Chen et al. (2022) to force the double inverse model. The modeling results are ambiguous due to the uncertainty inherent in the age model. Specifically, the reported data indicates a ~ 200 kyr lag in the onset of sea surface $\delta^{13}C$ excursion behind that of pCO_2 values. Consequently, the pCO_2 and $\delta^{13}C_{as}$ excursions last for 600 and 400 thousand years, respectively (Chen et al., 2022). To explore the impact of chronological uncertainty on modeling outcome, we execute two sets of experiments, where the CIE and the carbon emissions both last for ~400 (KGB1) or 600 kyr (KGB2).

Our inverse modeling results show that cumulative carbon emissions from KGB1 (9106 Gt C) are ~15% lower than those from KGB2 (10,494 Gt C) (Fig. 3c; Table S1). The noticeable difference suggests that the double-inversion results are sensitive to the selection of the age model. The higher cumulative carbon emissions in KGB2 can be attributed to more carbon removal through the silicate weathering feedback mechanisms under longer CIE duration scenarios. With total carbon release of similar order at a longer interval, the carbon emission rates during KGB from both experiments (~0.01–0.02 Gt C/yr) are one order of magnitude smaller than those during the PTB (~0.2 Gt C/yr). Correspondingly, the temperature increase is relatively modest, with a rise of ~3 °C over the 400 kyr period. Additionally, our inverse model also suggests a flux-weighted $\delta^{13}C$ source of −18.2‰ (KGB1) or − 23‰ (KGB2), which is consistent with previous estimate (−19‰; Chen et al., 2022) and implies the oxidation of organic sediments as the carbon source. The slower emission rates and slightly more ^{13}C-depleted source suggest mechanistic dissimilarities between the KGB and the PTB.

Our results further highlight two features regarding the carbon emission trajectory that are not identified in the previous work (Chen et al., 2022). Firstly, a gradual decrease in $\delta^{13}C_{source}$ with time is diagnosed (Fig. 3d and S4), indicating changing carbon sources across the KGB. Nonetheless, we place limited confidence in the precise values for each interval, as the pCO_2 and $\delta^{13}C_{as}$ data used here are derived from smoothed results and have large uncertainties (Chen et al., 2022). Nevertheless, a shift in the degassing mechanism across the KGB is plausible, but it necessitates further evidence to confirm. Secondly, the

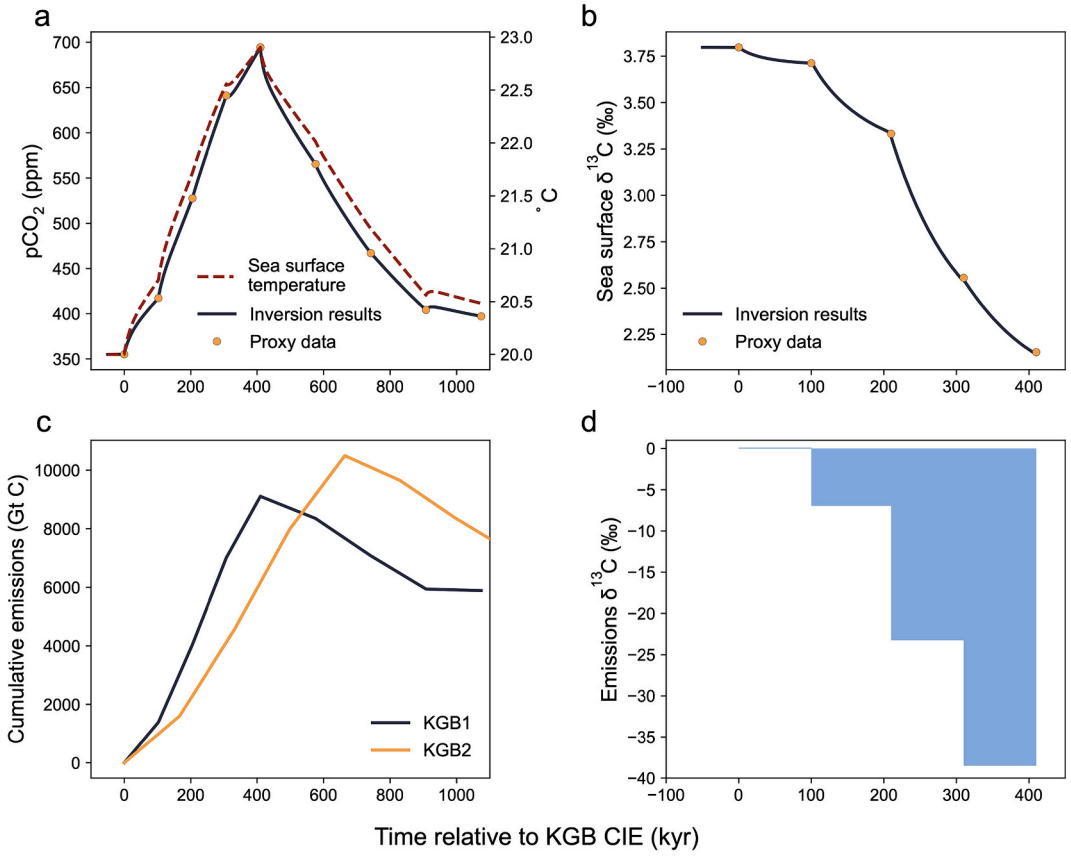

Fig. 3. KGB1 modeling results. a, b, Modeling pCO_2, sea surface temperature and $\delta^{13}C$ results from the inversion-derived carbon emission trajectories for the experiment KGB1. Yellow symbols in a and b denote the smoothing proxy records, which are used as input in the iLOSCAR inverse model (Chen et al., 2022). c, d, Inversion cumulative emission rates (KGB1 and KGB2) and source $\delta^{13}C$ (KGB1). Note that the results in b and d only span the CIE interval. (For interpretation of the references to colour in this figure legend, the reader is referred to the web version of this article.)

pCO_2 recovery following the peak CIE occurs more rapidly than expected if solely attributed to removal through silicate weathering alone, necessitating the presence of a negative carbon emission. KGB is also accompanied by an estimated 20% increase in seafloor anoxia areal extent, as inferred from uranium isotopes (Chen et al., 2022). Seafloor anoxia favors the burial and preservation of organic carbon. It also enhances the phosphorus remineralization and elevates the dissolved phosphorus concentration in the surface ocean, which in turn will boost the primary production and lead to greater organic carbon preservation (Komar and Zeebe, 2017; Papadomanolaki et al., 2022a; Slomp and Van Cappellen, 2007). Therefore, we hypothesize that the negative emissions diagnosed by our model likely represent enhanced organic carbon burial. This process removes carbon from the surface Earth system and expedites the recovery of pCO_2 levels.

6. Summary and outlook

The newly developed iLOSCAR model is capable of replicating the forward mode from the original LOSCAR model and executing the double-inversion experiment efficiently across various timescales. The close alignment of double-inversion results between iLOSCAR and cGENIE for geologic carbon perturbation events is not surprising, given the LOSCAR model encompasses most essential processes involved in the long-term carbon cycle (Zeebe, 2012). Hence, the iLOSCAR model presents itself as a reliable and efficient alternative to the complex cGENIE model, particularly when concentrating on the long-term carbon cycle at a basin-to-global scale. Furthermore, by utilizing the iLOSCAR inverse model, we offer novel insights into the emission characteristics during the KGB that were previously unexplored.

We also wish to emphasize the dynamic and continuously updatable nature of iLOSCAR. For instance, users are encouraged to reach out to us for discussions on how to modify parameters that are currently inaccessible via the web-based interface. Should certain modification emerge as common requests, we can update the model structure to enable adjusting these parameters directly from the interface. Moreover, the degree to which modeling results can approximate the true conditions in the geological history depends on both the quality of proxy data and the reliability of the model settings. A limitation for the current double-inversion method, whether iLOSCAR- or cGENIE-based, is that it can only inversely calculate the carbon emission rate from one single proxy (e.g., pCO_2 or pH_{as}). While it can perfectly match the target records, the model results of other carbon system variables are not guaranteed to align well with observations. It is becoming increasingly common to have multiple proxy records available for a single hyperthermal event, particularly for intensely studied events such as the PETM and PTB. Consequently, future versions of iLOSCAR are under development to offer an inverse function capable of deriving the optimal emission trajectory from multiple proxies.

CRediT authorship contribution statement

Shihan Li: Conceptualization, Data curation, Methodology, Software, Visualization, Writing – original draft. **Richard E. Zeebe:** Investigation, Methodology, Software, Writing – review & editing. **Shuang Zhang:** Conceptualization, Funding acquisition, Investigation, Methodology, Project administration, Software, Writing – review & editing.

Declaration of competing interest

The authors declare that they have no known competing financial interests or personal relationships that could have appeared to influence the work reported in this paper.

Data availability

All study data and coding files included in the article can be found in author's Github profile: https://github.com/Shihan150/iloscar. To use the iLOSCAR model via its web-based interface, it is mandatory to install Anaconda or Miniconda. Detailed guidelines for installing and initiating the model are also provided.

Acknowledgments

We thank Dr. Jitao Chen and Dr. Daoliang Chu for generously sharing the proxy data. We also thank Dr. Alexander J. Krause and one anonymous reviewer for their detailed and insightful comments that helped improve the manuscript and the model tutorial. Portions of this research were conducted with the advanced computing resources provided by Texas A&M High Performance Research Computing. This study is financially supported by the NSF (grant number: EAR-2241039), the GSA Graduate Student Research Grant, and the Schlanger Ocean Drilling Fellowship (funded by the US Science Support Program for the International Ocean Discovery Program). REZ acknowledges support from the US NSF (award OCE20-48436).

Appendix A. Supplementary data

Supplementary data to this article can be found online at https://doi.org/10.1016/j.gloplacha.2024.104413.

References

Adloff, M., Greene, S.E., Parkinson, I.J., Naafs, B.D.A., Preston, W., Ridgwell, A., Lunt, D. J., Castro Jiménez, J.M., Monteiro, F.M., 2020. Unravelling the sources of carbon emissions at the onset of Oceanic Anoxic Event (OAE) 1a. Earth Planet. Sci. Lett. 530, 115947 https://doi.org/10.1016/j.epsl.2019.115947.

Alefeld, G.E., Potra, F.A., Shi, Y., 1995. Algorithm 748: enclosing zeros of continuous functions. ACM Trans. Math. Softw. 21, 327–344. https://doi.org/10.1145/210089.210111.

Bowen, G.J., Maibauer, B.J., Kraus, M.J., Röhl, U., Westerhold, T., Steimke, A., Gingerich, P.D., Wing, S.L., Clyde, W.C., 2015. Two massive, rapid releases of carbon during the onset of the Palaeocene–Eocene thermal maximum. Nat. Geosci. 8, 44–47. https://doi.org/10.1038/ngeo2316.

Chen, J., Montañez, I.P., Zhang, S., Isson, T.T., Macarewich, S.I., Planavsky, N.J., Zhang, F., Rauzi, S., Daviau, K., Yao, L., Qi, Y., Wang, Y., Fan, J., Poulsen, C.J., Anbar, A.D., Shen, S., Wang, X., 2022. Marine anoxia linked to abrupt global warming during Earth's penultimate icehouse. Proc. Natl. Acad. Sci. 119, e2115231119 https://doi.org/10.1073/pnas.2115231119.

Clarkson, M.O., Stirling, C.H., Jenkyns, H.C., Dickson, A.J., Porcelli, D., Moy, C.M., Pogge von Strandmann, P.A.E., Cooke, I.R., Lenton, T.M., 2018. Uranium isotope evidence for two episodes of deoxygenation during Oceanic Anoxic Event 2. Proc. Natl. Acad. Sci. 115, 2918–2923. https://doi.org/10.1073/pnas.1715278115.

Cox, A.A., Keller, C.B., 2023. A Bayesian inversion for emissions and export productivity across the end-cretaceous boundary. Science 381, 1446–1451. https://doi.org/10.1126/science.adh3875.

Cui, Y., Kump, L.R., Ridgwell, A.J., Charles, A.J., Junium, C.K., Diefendorf, A.F., Freeman, K.H., Urban, N.M., Harding, I.C., 2011. Slow release of fossil carbon during the Palaeocene–Eocene Thermal Maximum. Nat. Geosci. 4, 481–485. https://doi.org/10.1038/ngeo1179.

Dunkley Jones, T., Manners, H.R., Hoggett, M., Kirtland Turner, S., Westerhold, T., Leng, M.J., Pancost, R.D., Ridgwell, A., Alegret, L., Duller, R., 2018. Dynamics of sediment flux to a bathyal continental margin section through the Paleocene–Eocene Thermal Maximum. Clim. Past 14, 1035–1049.

Edwards, N.R., Marsh, R., 2005. Uncertainties due to transport-parameter sensitivity in an efficient 3-D Ocean-climate model. Clim. Dyn. 24, 415–433. https://doi.org/10.1007/s00382-004-0508-8.

Fan, J., Shen, S., Erwin, D.H., Sadler, P.M., MacLeod, N., Cheng, Q., Hou, X., Yang, J., Wang, X., Wang, Y., Zhang, H., Chen, X., Li, G., Zhang, Y., Shi, Y., Yuan, D., Chen, Q., Zhang, L., Li, C., Zhao, Y., 2020. A high-resolution summary of Cambrian to early Triassic marine invertebrate biodiversity. Science 367, 272–277. https://doi.org/10.1126/science.aax4953.

Follows, M.J., Ito, T., Dutkiewicz, S., 2006. On the solution of the carbonate chemistry system in ocean biogeochemistry models. Ocean Model 12, 290–301. https://doi.org/10.1016/j.ocemod.2005.05.004.

Foster, G.L., Hull, P., Lunt, D.J., Zachos, J.C., 2018. Placing our current 'hyperthermal' in the context of rapid climate change in our geological past. Philos. Trans. R. Soc. A Math. Phys. Eng. Sci. 376, 20170086. https://doi.org/10.1098/rsta.2017.0086.

Goddéris, Y., Donnadieu, Y., Mills, B.J.W., 2023. What Models tell Us about the Evolution of Carbon sources and Sinks over the Phanerozoic. Annu. Rev. Earth Planet. Sci. 51, null. https://doi.org/10.1146/annurev-earth-032320-092701.

Gutjahr, M., Ridgwell, A., Sexton, P.F., Anagnostou, E., Pearson, P.N., Pälike, H., Norris, R.D., Thomas, E., Foster, G.L., 2017. Very large release of mostly volcanic carbon during the Palaeocene–Eocene Thermal Maximum. Nature 548, 573–577. https://doi.org/10.1038/nature23646.

Harper, D.T., Hönisch, B., Zeebe, R.E., Shaffer, G., Haynes, L.L., Thomas, E., Zachos, J.C., 2020. The magnitude of surface ocean acidification and carbon release during eocene thermal maximum 2 (ETM-2) and the Paleocene-Eocene thermal Maximum (PETM). Paleoceanogr. Paleoclimatol. 35 https://doi.org/10.1029/2019PA003699 e2019PA003699.

Heimdal, T.H., Jones, M.T., Svensen, H.H., 2020. Thermogenic carbon release from the Central Atlantic magmatic province caused major end-Triassic carbon cycle perturbations. Proc. Natl. Acad. Sci. 117, 11968–11974. https://doi.org/10.1073/pnas.2000095117.

Henehan, M.J., Edgar, K.M., Foster, G.L., Penman, D.E., Hull, P.M., Greenop, R., Anagnostou, E., Pearson, P.N., 2020. Revisiting the middle eocene climatic optimum "carbon cycle conundrum" with new estimates of atmospheric pCO2 from boron isotopes. Paleoceanogr. Paleoclimatol. 35 https://doi.org/10.1029/2019PA003713 e2019PA003713.

Hindmarsh, A., 1992. ODEPACK. A Collection of ODE System Solvers (No. ESTSC-000166CY00100; NESC-9935). Lawrence Livermore National Lab. (LLNL), Livermore, CA (United States).

Hönisch, B., Ridgwell, A., Schmidt, D.N., Thomas, E., Gibbs, S.J., Sluijs, A., Zeebe, R., Kump, L., Martindale, R.C., Greene, S.E., Kiessling, W., Ries, J., Zachos, J.C., Royer, D.L., Barker, S., Marchitto, T.M., Moyer, R., Pelejero, C., Ziveri, P., Foster, G. L., Williams, B., 2012. The geological record of ocean acidification. Science 335, 1058–1063. https://doi.org/10.1126/science.1208277.

Hull, P.M., Bornemann, A., Penman, D.E., Henehan, M.J., Norris, R.D., Wilson, P.A., Blum, P., Alegret, L., Batenburg, S.J., Bown, P.R., Bralower, T.J., Cournede, C., Deutsch, A., Donner, B., Friedrich, O., Jehle, S., Kim, H., Kroon, D., Lippert, P.C., Loroch, D., Moebius, I., Moriya, K., Peppe, D.J., Ravizza, G.E., Röhl, U., Schueth, J. D., Sepúlveda, J., Sexton, P.F., Sibert, E.C., Śliwińska, K.K., Summons, R.E., Thomas, E., Westerhold, T., Whiteside, J.H., Yamaguchi, T., Zachos, J.C., 2020. On impact and volcanism across the Cretaceous-Paleogene boundary. Science 367, 266–272. https://doi.org/10.1126/science.aay5055.

Isson, T.T., Zhang, S., Lau, K.V., Rauzi, S., Tosca, N.J., Penman, D.E., Planavsky, N.J., 2022. Marine siliceous ecosystem decline led to sustained anomalous early Triassic warmth. Nat. Commun. 13, 3509. https://doi.org/10.1038/s41467-022-31128-3.

Komar, N., Zeebe, R.E., 2016. Calcium and calcium isotope changes during carbon cycle perturbations at the end-Permian. Paleoceanography 31, 115–130.

Komar, N., Zeebe, R.E., 2017. Redox-controlled carbon and phosphorus burial: a mechanism for enhanced organic carbon sequestration during the PETM. Earth Planet. Sci. Lett. 479, 71–82. https://doi.org/10.1016/j.epsl.2017.09.011.

Krissansen-Totton, J., Catling, D.C., 2017. Constraining climate sensitivity and continental versus seafloor weathering using an inverse geological carbon cycle model. Nat. Commun. 8 (1), 1–15. https://doi.org/10.1038/ncomms15423.

Krissansen-Totton, J., Catling, D.C., 2020. A coupled carbon-silicon cycle model over Earth history: reverse weathering as a possible explanation of a warm mid-Proterozoic climate. Earth Planet. Sci. Lett. 537, 116181 https://doi.org/10.1016/j.epsl.2020.116181.

Landwehrs, J.P., Feulner, G., Hofmann, M., Petri, S., 2020. Climatic fluctuations modeled for carbon and sulfur emissions from end-Triassic volcanism. Earth Planet. Sci. Lett. 537, 116174 https://doi.org/10.1016/j.epsl.2020.116174.

Legg, S., 2021. IPCC, 2021: climate change 2021 - the physical science basis. Interaction 49, 44–45. https://doi.org/10.3316/informit.315096509383738.

Morice, C.P., Kennedy, J.J., Rayner, N.A., Winn, J.P., Hogan, E., Killick, R.E., Dunn, R.J. H., Osborn, T.J., Jones, P.D., Simpson, I.R., 2021. An updated assessment of near-surface temperature change from 1850: the HadCRUT5 data set. J. Geophys. Res. Atmos. 126 https://doi.org/10.1029/2019JD032361 e2019JD032361.

Papadomanolaki, N.M., Lenstra, W.K., Wolthers, M., Slomp, C.P., 2022a. Enhanced phosphorus recycling during past oceanic anoxia amplified by low rates of apatite authigenesis. Sci. Adv. 8, eabn2370. https://doi.org/10.1126/sciadv.abn2370.

Papadomanolaki, N.M., van Helmond, N.A.G.M., Pälike, H., Sluijs, A., Slomp, C.P., 2022b. Quantifying volcanism and organic carbon burial across Oceanic Anoxic Event 2. Geology 50, 511–515. https://doi.org/10.1130/G49649.1.

Ridgwell, A., Hargreaves, J.C., 2007. Regulation of atmospheric CO2 by deep-sea sediments in an Earth system model. Glob. Biogeochem. Cycles 21. https://doi.org/10.1029/2006GB002764.

Ridgwell, A., Hargreaves, J.C., Edwards, N.R., Annan, J.D., Lenton, T.M., Marsh, R., Yool, A., Watson, A., 2007. Marine geochemical data assimilation in an efficient Earth System Model of global biogeochemical cycling. Biogeosciences 4, 87–104. https://doi.org/10.5194/bg-4-87-2007.

Shen, Jun, Yin, R., Zhang, S., Algeo, T.J., Bottjer, D.J., Yu, J., Xu, G., Penman, D., Wang, Y., Li, L., Shi, X., Planavsky, N.J., Feng, Q., Xie, S., 2022a. Intensified continental chemical weathering and carbon-cycle perturbations linked to volcanism during the Triassic–Jurassic transition. Nat. Commun. 13, 299. https://doi.org/10.1038/s41467-022-27965-x.

Shen, Jiaheng, Zhang, Y.G., Yang, H., Xie, S., Pearson, A., 2022b. Early and late phases of the Permian–Triassic mass extinction marked by different atmospheric CO2 regimes. Nat. Geosci. 15, 839–844. https://doi.org/10.1038/s41561-022-01034-w.

Slomp, C.P., Van Cappellen, P., 2007. The global marine phosphorus cycle: sensitivity to oceanic circulation. Biogeosciences 4, 155–171. https://doi.org/10.5194/bg-4-155-2007.

Sun, Y., Joachimski, M.M., Wignall, P.B., Yan, C., Chen, Y., Jiang, H., Wang, L., Lai, X., 2012. Lethally Hot Temperatures during the early Triassic Greenhouse. Science 338, 366–370. https://doi.org/10.1126/science.1224126.

Wang, W., Zhang, F., Zhang, S., Cui, Y., Zheng, Q., Zhang, Y., Yuan, D., Zhang, H., Xu, Y., Shen, S., 2023. Ecosystem responses of two Permian biocrises modulated by CO2 emission rates. Earth Planet. Sci. Lett. 602, 117940 https://doi.org/10.1016/j.epsl.2022.117940.

Wu, Y., Chu, D., Tong, J., Song, Haijun, Dal Corso, J., Wignall, P.B., Song, Huyue, Du, Y., Cui, Y., 2021. Six-fold increase of atmospheric pCO2 during the Permian–Triassic mass extinction. Nat. Commun. 12, 2137. https://doi.org/10.1038/s41467-021-22298-7.

Wu, Y., Cui, Y., Chu, D., Song, H., Tong, J., Dal Corso, J., Ridgwell, A., 2023. Volcanic CO2 degassing postdates thermogenic carbon emission during the end-Permian mass extinction. Sci. Adv. 9, eabq4082. https://doi.org/10.1126/sciadv.abq4082.

Zeebe, R.E., 2012. LOSCAR: long-term ocean-atmosphere-sediment carbon cycle reservoir model v2. 0.4. Geosci. Model Dev. 5, 149–166.

Zeebe, R.E., Ridgwell, A., Zachos, J.C., 2016. Anthropogenic carbon release rate unprecedented during the past 66 million years. Nature Geosci 9, 325–329. https://doi.org/10.1038/ngeo2681.

Zeebe, R.E., Zachos, J.C., Caldeira, K., Tyrrell, T., 2008. Carbon Emissions and Acidification. Science 321, 51–52. https://doi.org/10.1126/science.1159124.

Zeebe, R.E., Zachos, J.C., Dickens, G.R., 2009. Carbon dioxide forcing alone insufficient to explain Palaeocene–Eocene Thermal Maximum warming. Nat. Geosci. 2, 576–580.